M2LW-19OR0402028

Light Water Reactor Sustainability Program

Elucidating the grain-orientation dependent oxidation rates of austenitic stainless steels

September 2019

U.S. Department of Energy

Office of Nuclear Energy

M2LW-19OR0402028

Elucidating the grain-orientation dependent oxidation rates of austenitic stainless steels

Shiqi Dong ([1,2]), Xin Chen ([1]), Erika Callagon La Plante ([1]), Maxim Gussev ([3]), Keith Leonard ([3]), Gaurav Sant ([1,2,4,5,])*

[1] Laboratory for the Chemistry of Construction Materials (LC[2]), Department of Civil and Environmental Engineering, University of California, Los Angeles, CA, USA
[2] Department of Materials Science and Engineering, University of California, Los Angeles, CA, USA
[3]Oak Ridge National Laboratory, Oak Ridge, TN, USA
[4] California Nanosystems Institute (CNSI), University of California, Los Angeles, CA, USA
[5] Institute for Carbon Management (ICM), University of California, Los Angeles, CA, USA

** Corresponding author: Gaurav Sant, Phone: (310) 206-3084, Email: gsant@ucla.edu*

September 2019

Prepared for the
U.S. Department of Energy
Office of Nuclear Energy
Light Water Reactor Sustainability
Materials Research Pathway

This page intentionally left blank

EXECUTIVE SUMMARY

Overview: Stainless steel, an austenitic alloy forms critical core-internal components in nuclear power plants. Expectedly, stainless steel presents complex polycrystalline microstructures, such that an exposed steel surface features a multiplicity of grains which too feature diverse grain orientations. Significantly, grain orientation-dependent oxidation (dissolution-corrosion) rates have been observed for austenitic alloys in nuclear reactor environments, suggesting crystallographic control of such reaction processes. To better understand these observations, the active and transpassive oxidation behaviors of an austenitic 316L stainless steel were investigated using vertical scanning interferometry (VSI). The oxidation rates of more than 100 grains were measured and related to their crystallographic orientations as identified using electron backscatter diffraction (EBSD). The oxidation rates follow a scaling that is given by: {001} < {101} < {111} for 316L undergoing both active and transpassive oxidation, such that a higher dangling-bond density led to slower oxidation. Further, an increasing surface energy that scales as {111} < {101} < {001} promoted the adsorption of inert species that increased the activation energy of oxidation and, in turn, decreased alloy corrosion rates. These insights provide improved understanding into the crystallographic controls of oxidation processes, and thereby suggest processing pathways for enhancing the oxidation resistance of stainless steels.

Implications: The outcomes of this work provide new understanding of how alloy microstructure (i.e., the crystallographic orientation of grains on the exposed surfaces of an alloy), and therefore, the nature of its processing may render stainless steel, and core-internal components fabricated therefrom, susceptible to corrosion. This is especially important from the perspective of understanding how changes in the cooling water chemistry that may results from switching of the alkalization agent (i.e., switching LiOH by KOH) may alter, or affect electrochemical processes such as corrosion. New knowledge of this nature is prerequisite to understand and predict, and to develop new methods to assess degradation that may result in stress corrosion cracking, under conditions of both radiation exposure, and in radiation-free environments that are relevant to nuclear power plants.

This page intentionally left blank

ACKNOWLEDGEMENTS

The authors acknowledge financial support for this research from the U.S. Department of Energy, Office of Nuclear Energy, Light Water Reactor Sustainability (LWRS) Program through the Oak Ridge National Laboratory operated by UT-Battelle LLC (Contract #: 4000154999). The contents of this paper reflect the views and opinions of the authors who are responsible for the accuracy of data presented. This research was carried out in the Laboratory for the Chemistry of Construction Materials (LC^2) and the California Nanosystems Institute at UCLA. As such, the authors gratefully acknowledge the support that has made these facilities and their operations possible.

This page intentionally left blank

CONTENTS

This page internationally left blank

1. Introduction

Austenitic alloys such as 304L and 316L stainless steels, and nickel-based alloys are often used in core-reactor internal components in nuclear power plants[1]. These alloys all exhibit a face-centered-cubic (FCC) lattice structure and feature excellent high-temperature oxidation resistance[2]. However, degradation of these alloys, e.g., due to degradation mechanisms such as stress corrosion cracking (SCC) renders these components susceptible to hyperbolic failure, and to violate the “leak-before-break” criterion[3]. So far, considerable efforts have been made to uncover the impact of grain boundary structures on SCC susceptibility[4–7]. However, less is known about how crystallographic orientations influnces electrochemical (i.e., oxidation) degradation of such alloys.

Crystallographic orientation is well-known to affect surface reactions including: dissolution, adsorption, oxidation, and pitting for both single crystals and polycrystalline materials[8–12]. In each of these cases, the anisotropy of atomic arrangements on the surface results in spatially and temporally non-uniform reaction kinetics – even for chemically equivalent reactions – amongst grains with different orientations. For example, for austenitic alloys oxidized in simulated reactor environments, the morphology and thickness of the oxide layers formed show a strong dependence on the orientation of underlying grains[13]. Furthermore, in the case of 316L stainless steel, the substantial difference in oxidation rates between diversely oriented grains results in the formation of a “step structure” at grain boundaries that could lead to crack initiation and a reductions in service-life[14].

Many studies have attributed the dependence of corrosion rates on grain orientation to differences in the surface energy[15–17]. However, in the majority of studies, grain-specific corrosion behavior is examined only for a few grains which feature a limited diversity of Miller surface indices[16–19]. Furthermore, corrosion susceptibility is often ranked through the analysis of line profiles which show a height difference for adjacent grains[20,21], i.e., instead of presenting a spatially averaged corrosion rate that applies to the entire exposed surface of a grain. Therefore, this study undertakes analyses of a large number of grains (>100 unique grains) to reveal statistically relevant insights into how grain orientation affects oxidation rates. As such, the effects of crystallographic orientation on both active (i.e., potential-free) and transpassive (i.e., potential-promoted) oxidation of AISI 316L stainless steel were systematically examined by coupling topographical measurements using vertical scanning interferometry (VSI) with microstructural analyses using electron backscatter diffraction (EBSD). The VSI analysis allows access to representative scanning areas (0.5 mm x 0.5 mm) at lateral and height resolutions of ±80 nm and ±2 nm, respectively, allowing superposition of orientation-specific oxidation rates onto an EBSD-derived grain orientation map. The outcomes reveal the effects of grain orientation on corrosion sensitivity and its mechanistic origins.

2. Experimental

2.1 Sample preparation

A commercially available 316L stainless steel (McMaster-Carr) was used. The elemental composition of the steel used is noted in Table 1. Herein, the steel sections were solution annealed using a vacuum tube furnace at 1000 °C for 1 h and then furnace-cooled to room temperature. Annealing produced a monophasic austenitic microstructure with easily distinguishable grains. The annealed steel was then sectioned in to smaller coupons with dimensions of 6mm in diameter and 6 mm in height. Thereafter, the coupons were embedded in epoxy, and then wet-polished using SiC abrasives and diamond paste, and finally polished using a 50 nm colloidal silica suspension.

Table 1. The chemical composition of the 316L stainless steel used (mass %)

Fe	Cr	Ni	Mo	Mn	N	C	Si	Cu
bal.	16.630	10.070	2.080	1.530	0.054	0.025	0.550	0.490

2.2 Crystallographic analysis

The crystallographic orientations of the grains were determined using a SEM (TESCAN MIRA3) equipped with an EBSD detector (Oxford ULTIM MAX). The acceleration voltage and step size used were 20 kV and 0.5 µm, respectively. The EBSD patterns were analyzed using OIM Analysis® and the MTEX toolbox in MATLAB® R2017b[22,23]. The averaged Euler angles over all pixels within individual grains provided by the EBSD analyses were used to represent the rotations for each grain. The Miller indices, *h, k, l* of individual grains were computed using:

$$h = n \cdot sin\varphi_2 \cdot sin\Phi \quad (1)$$

$$k = n \cdot cos\varphi_2 \cdot sin\Phi \quad (2)$$

$$l = n \cdot cos\Phi \quad (3)$$

where φ_2 and Φ are the Bunge Euler angles and *n* is a scaling factor to attain integer indices.[24]

2.3 Oxidation (corrosion) rate analysis

Active corrosion was induced by immersing the steel coupon's surface in a 0.5 M H_2SO_4 + 0.1 M LiCl solution for up to 80 h in a temperature-controlled chamber (45 ± 0.2 °C). Transpassive corrosion was induced by immersing the surface of the steel coupon in a 10 mass % oxalic acid solution for 45 s while imposing a constant current density of 1 A/cm^2. The surface topographies of corroding sections were examined using a Zygo NewView 8200 vertical scanning interferometry (VSI). A 20× Mirau (numerical aperture, NA = 0.4) and a 100× (NA = 0.55) interferometric objectives were used. The former, and latter objectives provide spatial resolutions (i.e., pixel size in *x* and *y* directions) of 410 nm µm and 80 nm, respectively. The vertical (height) resolution of both objectives is

equivalent and on the order of 2 nm. The surface topographies were analyzed using Gwyddion[25]. The surfaces of the steel coupons were partially covered by a peelable silicone mask (Silicone Solutions SS-380) to preserve unreacted surfaces. The height change, i.e. surface retreat, of the corroded (oxidized) steel surface vis-à-vis the pristine steel surface was determined by reference with the unreacted steel surface that is preserved beneath the silicone mask[26]. The corrosion rate (R_c, nm/s) is simply represented, as a spatial average of all the pixels that constitute a single grain as: $\Delta h/\Delta t$, where, Δh is the surface retreat and t is time period over which oxidation occurred.

3. Results and discussion

3.1 Grain orientation impacts on the potential-free active corrosion of 316L

The microstructure of as-polished 316L stainless steel was examined using EBSD and shown in **Figure 1**. The solution-annealed sample only consists of austenite grains and is free from deformation-induced features. Over 100 grains were identified within the selected area, with their orientations mapped by EBSD as shown in **Figure 1a**. The orientations of these grains are plotted in the inverse pole figure (IPF) triangle (**Figure 1b**) which shows a diversified orientation distribution within the examined area.

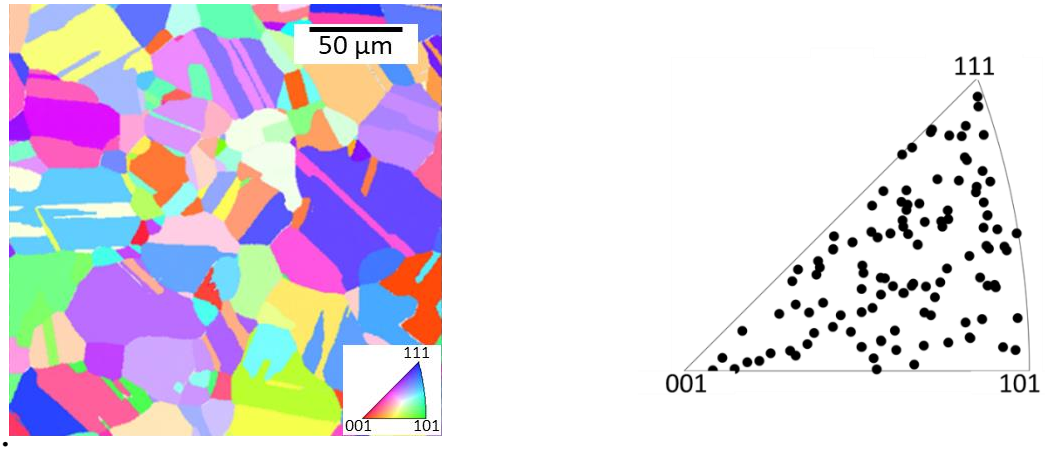

(a) **(b)**

Figure 1: EBSD analysis showing the microstructure of the solution-annealed 316L stainless steel surface: **(a)** The grain orientation map of the analyzed surface, with the color code shown in the inverse pole figure (IPF) as the inset, and **(b)** The collective orientation distribution of grains examined herein.

First, unstimulated (*potential-free*) corrosion studies were carried out by immersing the 316L steel in a 0.5 M H_2SO_4 + 0.1 M NaCl solution at 45 °C for up to 80 hours. The equilibrium potential of 316L in the solution is around -400 $mV_{Ag/AgCl}$[27], equivalent to about -150 mV_{SHE} which is within with the range of stainless steels under simulated reactor environments[28]. In this environment, 316L is expected to undergo active

corrosion and be oxidized to lower valence oxidation products (e.g., Fe^{2+}, Cr^{3+}, etc.)[29,30]. Subsequently, the actively corroded surface was characterized and the corrosion rates were determined using VSI (**Figure 2**). The topography map (**Figure 2a**) of the same area as mapped by EBSD shows that the polished surface has an overall height variance of around ±80 nm. The height difference between adjacent grains is on the order of a few nanometers. Following immersion in a 0.5 M H_2SO_4 + 0.1 M NaCl solution at 45 °C for 20 hours the surface recessed by up to 2.0 µm (**Figure 2b**), suggesting the onset of active corrosion. The morphology of the corroded surface indicates that active corrosion occurred in two forms: localized corrosion and the general surface retreat. Localized corrosion sites resemble shallow pits and are represented by darker basins in the topography map. The presence of basins typically denote transition from pitting to general corrosion following the breakdown of an air-formed passive film[26,31]. The rest of the steel surface experienced general corrosion. Surface recession rates in these general corrosion areas are lower, but show a more evident dependence on grain orientation. For example, the “step” structure resulting from distinct corrosion rates of differently oriented grains is seen in **Figure 2(c)**. The height difference between the adjacent grains which is on the order of ±5 nm prior to solution exposure increased to around 1.0 µm after 20 h of active corrosion in the immersion solution.

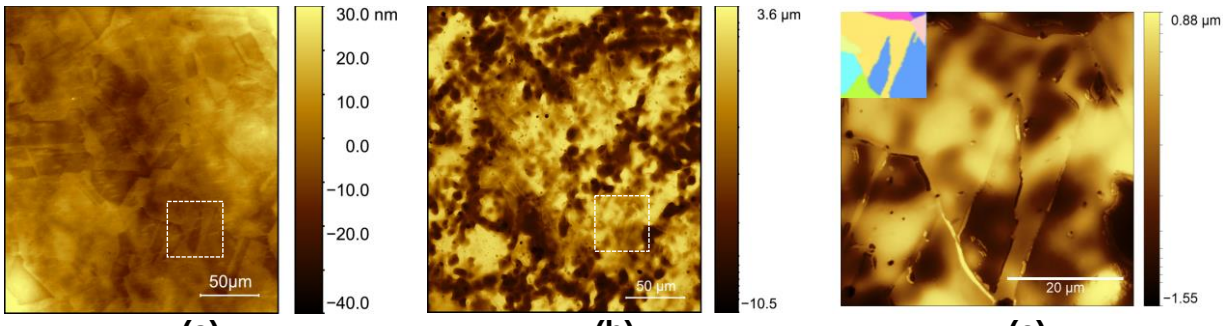

Figure 2: Representative VSI topography images of **(a)** an as-polished 316L stainless steel and **(b)** a corroded steel surface following corrosion reaction for 20 h. **(c)** The “step structure” between adjacent grains resulted from the difference in crystallographic orientation. An EBSD map of the same area is shown as inset.

The average height of the steel surface progressively recessed with prolonged immersion as shown in **Figure 3a**. Note that the rate from t = 0 h to t = 20 h is somewhat faster than those at longer immersion times. The faster corrosion rate at the initial stage can be explained by the coupling of pitting and general corrosion. The longer term (dissolution, corrosion) rate, i.e., after 20 hours is similar to that reported by others[32]. Therefore, for the sake of examining the steady-state rate, the early rate, is not considered. The surface recession after 20 hours reveals an active corrosion rate of 0.0194 µm/h or 170 µm/year. This value is in agreement with previous studies of the active corrosion rate of 316L under similar conditions[33].

Quantitative analysis of the average surface height of individual grains was enabled by overlapping the VSI topographies and EBSD microstructure maps. The frequency

distributions of the grain-average surface height (**Figures 3b**) were fitted using a Gaussian function of the form:

$$f_{(x)} = a \cdot \exp\left[-\left(\frac{x-b}{c}\right)^2\right] \quad (4)$$

where *x* is the height change, *a*, *b*, and *c* are fitting parameters denoting the scaling factor for frequency, mean height change, and the spread in height change, respectively. Up to 20 hours of corrosion, the average surface retreat (i.e., as averaged over the exposed surface area of the grain) is around 0.82 µm (**Figure 3b**) and the variance in height of most grains is ±0.35 µm. At a later time, the dissolution rates of the differently oriented grains increasingly diverged. The broadening of the distribution profiles over time implies that the grains, which feature a variety of surface orientations, corroded at different rates.

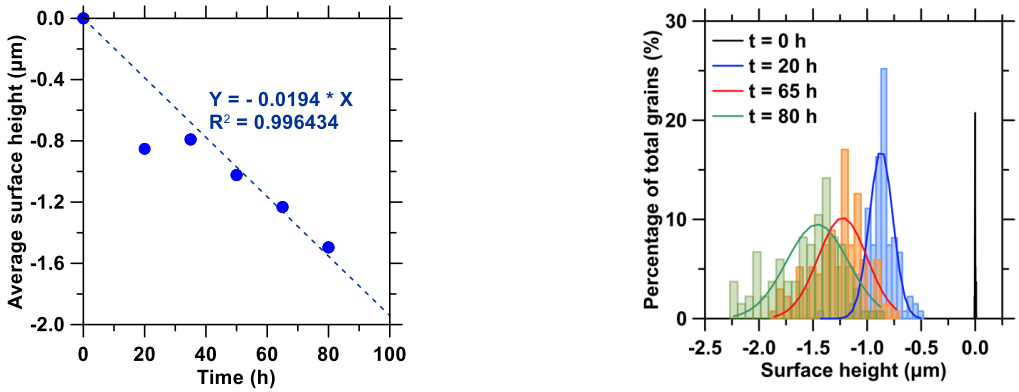

Figure 3: (a) The average surface height change of 316L stainless steel surface over time. The dashed line indicates the best-fit line for the data excluding the point at t = 20 h. **(b)** The grain averaged surface height change frequency distributions of surfaces corroded for different extents of time including 20 h, 65 h, and 80 h. The black curves represent the surface height change frequency distribution of the as-polished steel surface, which centered at 0.0 µm (mean), and spread over a range of 20 nm (standard deviation).

3.2 Grain orientation impacts on the potential-induced transpassive corrosion of 316L stainless steel

The "potential-free" corrosion of 316L revealed that corrosion rates are correlated with crystallographic orientation. But herein, the "step-structure" is less pronounced due to the formation of recessed basin areas. To better understand 316L corrosion under electrochemical stimulation, a potential was applied to the steel surface to induce transpassive corrosion. When a high anodic potential is applied to steel, the surface-proximate passivation layer breaks down instantly, and the steel dissolves transpassively into high valence species including as Fe^{3+}, $HCrO_4^-$, etc.[29] Although these oxidation products differ from those produced during the initial oxidation of stainless steel in reactor environments, they form, in time, due to interactions with oxidants that represent radiolytic products (e.g., H_2O_2)[34,35,36]. Therefore, an area within

the 316L sample enclosing about 200 randomly oriented grains was analyzed under conditions of applied potential (**Figure 4a-b**). Following transpassive corrosion in oxalic acid, the surface topography showed prominent (grain) contours (**Figure 4c**) arising from the formation of steps at grain boundaries with the average surface height having recessed by about 1.1 µm in just 45 seconds. Since the height variations within individual grains are much smaller compared to the actively corroded surface, the variance of ±0.25 µm as shown in **Figure 4d** is dominantly produced on account of the differences in corrosion rate among grains which feature diverse orientations.

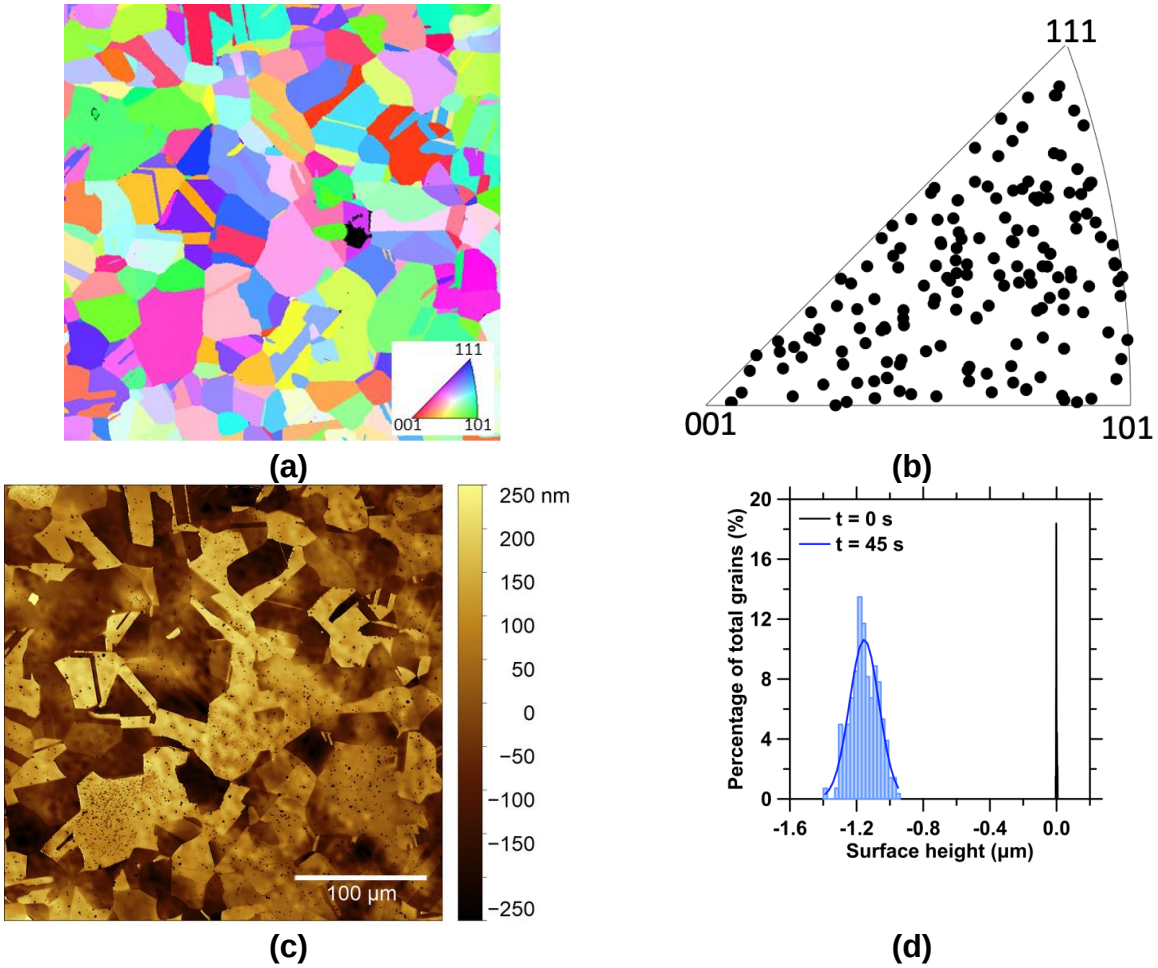

Figure 4: EBSD analysis of the microstructure of the solution-annealed 316L stainless steel surface showing: **(a)** grain orientation map with the color code shown in the inverse pole figure (IPF) as inset, and **(b)** collective orientation distribution of around 200 grains investigated herein. **(c)** The same area after transpassive corrosion in oxalic acid, and **(d)** The surface height distribution showing corrosion rate variations as affected by crystallographic orientation of the surficial grains.

3.3 Correlating corrosion rates with grain orientations

By combining EBSD and VSI analyses, the corrosion rates of individual grains were extracted and then correlated with their respective. Both the active and transpassive

corrosion rates of grains were presented in IPF plots. The scatter in active corrosion rates **(Figure 5a)** is unexpectedly, substantial. This can be attributed to the formation of the orientation-independent basins, which contribute to the grain's average corrosion rate. Nevertheless, orientation dependence is evident in the dashed circles which show a few grains that are oriented close to the basis directions (i.e., [001], [101], and [111]). Indeed, the corrosion rates of these grains scaled as: {001} < {101} < {111}. In addition, the orientation-specific corrosion rate was examined as a function of the angle (θ) between the surface normal and the [111] basis (**Figures 5b**) computed as follows:

$$\theta_{(111)} = cos^{-1}\left(\frac{h+k+l}{\sqrt{3}\cdot\sqrt{h^2+k^2+l^2}}\right) \quad (5)$$

where h, k, l are the Miller indices of the surface normal. Interestingly, despite the large scatter, the corrosion rates show a decreasing trend as $\theta_{(111)}$ increases.

Consistent with the active corrosion rate map, the transpassive corrosion rate map (**Figure 5c**) shows that the grains strongly associated with the {111} planes rapidly dissolve, whereas the grains oriented close to the {001} planes show the highest resistance to corrosion. The scattering in the grain-averaged corrosion rates is significantly reduced, so that a more pronounced linear trend in corrosion rates is seen in grains with orientations intermediate between {111} and {001} (**Figure 5d**). In general, the transpassive corrosion rates confirm that the general corrosion susceptibility ranks from {001} grains having the lowest to {111} grains having the highest. Taken together, these findings indicate that crystallographic control of corrosion rates is, in fact, independent of the applied potential and the nature of corrosion products that form.

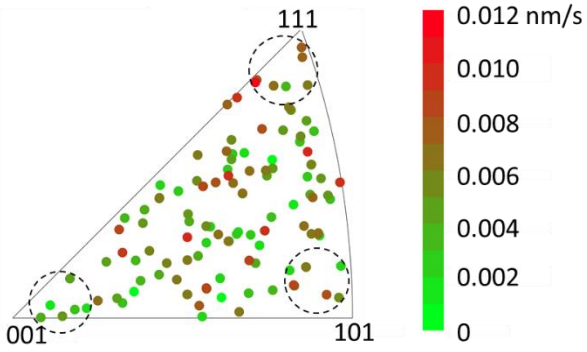

(a)

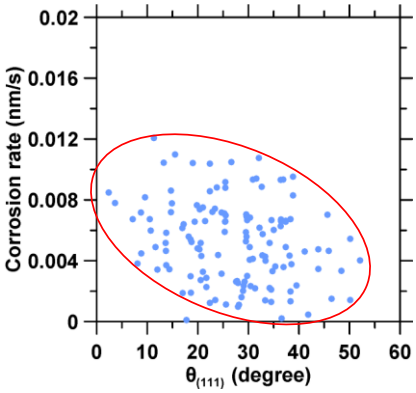

(b)

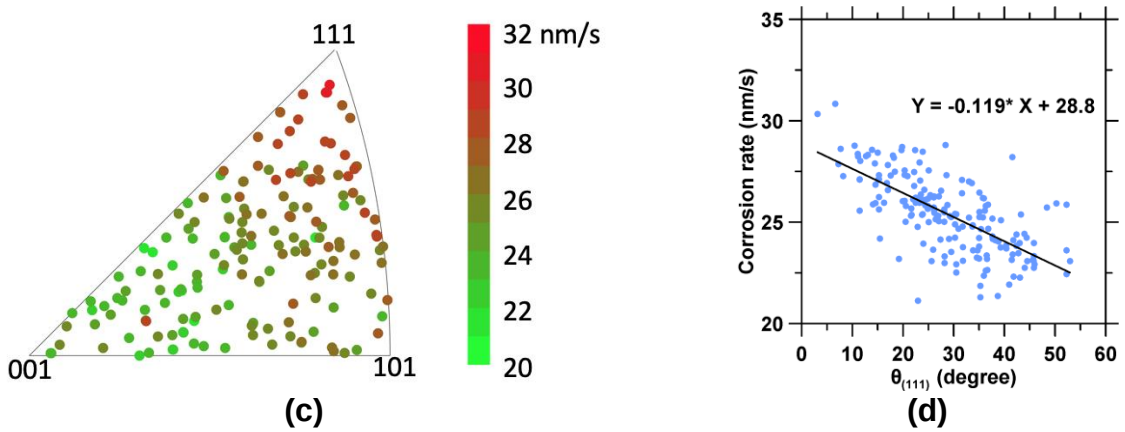

(c) **(d)**

Figure 5: (a) Active and **(c)** transpassive corrosion rates plotted in inverse pole figures showing grain orientation dependence. **(b)** Active and **(d)** transpassive corrosion rates as a function of $\theta_{(111)}$.

3.4 Effects of surface and activation energies on corrosion rates

The initial step in corrosion is postulated to require the mass transfer (dissolution) of the alloy. Therefore, in analogy to a dissolution process the corrosion rate is governed by the energy needed to overcome the energy barrier between the reactants and products, i.e. the activation energy (ΔG^a), as in the Arrhenius-type kinetics[37–39]. The corrosion process, in which the steel surface oxidizes to aqueous ions, involves removal of surface layers and exposing the underlying planes. Thus, some of the energy cost for corrosion is associated with overcoming interatomic forces between: (a) the surface and the underlying layers, and (b) bonds between atoms within a given layer. Such energy demands vary in relation to the backbond density, which reflect the number-of-bonds to be broken to dissolve one surface layer. The anisotropic arrangements of surface atoms among grains which produces different energy magnitudes of surface-to-surface, and atom-to-atom bonding[16,17,20]. Assuming general corrosion proceeds normal to the grain surface (i.e., in an exfoliation manner), the number of backbonds is equal to the number of dangling bonds on the existing surface. The surface energy is defined as the excess free energy resulting from dangling bonds[40] and has been previously estimated as follows[41–44]:

$$Surface\ Energy = 2\frac{2|h|+|k|}{\sqrt{h^2+k^2+l^2}} \cdot \frac{E_b}{d_0} \quad (6)$$

where *h,k,l* are the surface plane indices of a given grain and arranged as $h \geq k \geq l$, E_b is the bond energy for a representative atomic bond and d_0 is the length of metallic bonds[20]. In some cases, the bond energy is also referred to as the cohesion energy per bond[45]. Thus, E_b and d_0 are constants for a given material and independent of grain orientation assuming that alloying elements randomly occupy lattice sites on the grain surfaces and in the bulk. Therefore, for the same material, the surface energy is solely determined by the pre-factor proportional to the dangling bond density: $\frac{2|h|+|k|}{\sqrt{h^2+k^2+l^2}}$, which is an orientation-specific quantity. **Figures 6(a-b)** show the distribution of the calculated

pre-factor for grains featuring diverse orientations for both active and transpassive corrosion. It is noted that the {111} surface, which exhibited fastest corrosion also featured the lowest surface energy. These observations imply that the observed corrosion behavior results from the increase in activation energy with increasing backbond (and dangling bond) density. Thus, the {111} grains, although possessing the lowest surface energy, featured the highest tendency to corrode because of the relatively low activation energy required for their layer-by-layer exfoliation ($\Delta G^{a}_{(111)}$). The backbond density increases with increasing deviation from the {111} orientation, i.e., with increasing $\theta_{(111)}$, indicating that more bonds need to break to remove a surface layer. This results in a reduction in corrosion rates and is consistent with the observations shown in **Figure 5**. Based on the corrosion rates mapped in **Figure 5**, the orientation-dependent activation energy scaling that is given by: {001} > {101} > {111}, i.e., $\Delta G^{a}_{(001)} > \Delta G^{a}_{(101)} > \Delta G^{a}_{(111)}$.

Further, a system tends to minimize its surface energy via adsorption, and higher rates of adsorption are usually attained on surfaces having high surface energies[46,47]. The adsorption layer of inactive species (e.g., anions, hydrogen, and oxygen) structurally blocks the surface-solution interaction, and thus further also elevates the threshold energy and active energy of corrosion[48]. Significantly, previously measured adsorption rates of hydrogen on 304 stainless steel (FCC) follows the scaling: {001} > {101} > {111}[49]. The other study showed that the oxygen adsorption layer on nickel (FCC) {001} planes is more protective preventing further oxidation compared to that formed on {111} planes[48]. Therefore, the elevation in activation energy resulting from such adsorption layers follows the equivalent scaling: $\Delta G^{a}_{(001)} > \Delta G^{a}_{(101)} > \Delta G^{a}_{(111)}$, thus further increasing the activation energy for oxidation in high-surface energy orientations.

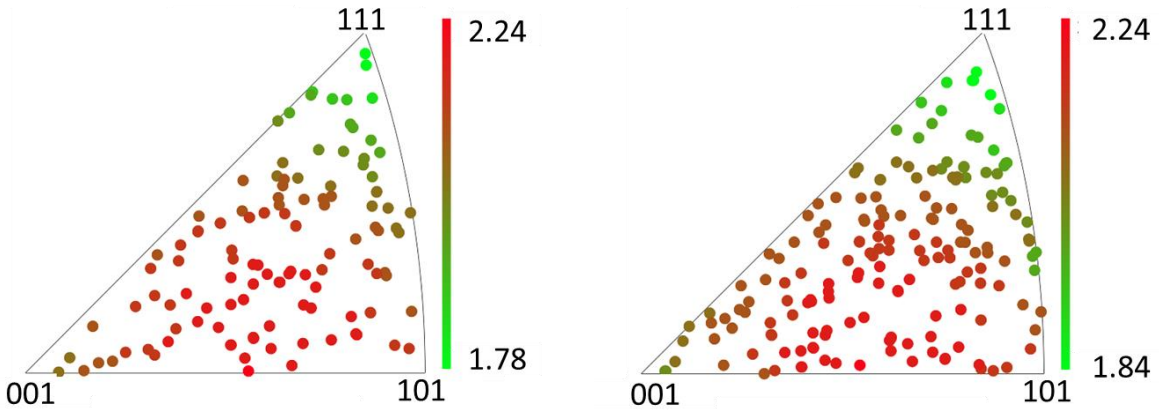

(a) **(b)**

Figure 6: The Calculated surface energy pre-factor, $\frac{2|h|+|k|}{\sqrt{h^2+k^2+l^2}}$, for alloy grains having various crystallographic orientations in experiments measuring: **(a)** active and **(b)** transpassive corrosion rates.

4. Conclusions

This work examined the active and transpassive corrosion rates of 316L stainless steel for hundreds of grains which featured diverse crystallographic orientations. The absolute active and transpassive corrosion rates were quantified by measuring the surface height retreat. The grain-specific corrosion rates, respectively, increase and then decrease as the surface plane progressively deviated from the [001] and [111] directions. Although the {111} planes has the lowest surface energy, they also contained fewer backbonds (and dangling bonds). Thus, the amount of energy that is needed to expose the underlying {111} planes (i.e., activation energy for oxidation) is lower compared to those for {001} and {101} grains. Favored adsorption at high surface energy planes further increases the activation energy. However, this model is less successful at explaining why {001} grains exhibit the lowest corrosion rates. This is likely on account of more complex orientation-dependent reactions such as surface reconstructions that are not considered herein.

Nevertheless, the approach presented herein is significant in that it established a credible correlation between grain orientation and general corrosion. This highlights a microstructural linkage to corrosion sensitivity and indicates that metallurgical processing that produces surface textures that exposes {001} planes is likely preferred to improve oxidation resistance. Moreover, it highlights that the orientation dependence (mismatch) of adjacent grains may cause the formation of “step structures” (see **Figure 2c**), which could result in stress concentration and localization in components subjected to mechanical loading. Not only could this result in the formation of weak planes, but it may also lead to an amplified tendency for stress-corrosion cracking (SCC) in such weakened regions.

5. References

(1) Cattant, F.; Crusset, D.; Féron, D. Corrosion Issues in Nuclear Industry Today. *Materials today* **2008**, *11* (10), 32–37.

(2) Murty, K. L.; Charit, I. Structural Materials for Gen-IV Nuclear Reactors: Challenges and Opportunities. *Journal of Nuclear Materials* **2008**, *383* (1–2), 189–195.

(3) Hertzberg, R. W.; Hauser, F. E. *Deformation and Fracture Mechanics of Engineering Materials*; American Society of Mechanical Engineers Digital Collection, 1977.

(4) King, A.; Johnson, G.; Engelberg, D.; Ludwig, W.; Marrow, J. Observations of Intergranular Stress Corrosion Cracking in a Grain-Mapped Polycrystal. *Science* **2008**, *321* (5887), 382–385.

(5) Gertsman, V. Y.; Bruemmer, S. M. Study of Grain Boundary Character along Intergranular Stress Corrosion Crack Paths in Austenitic Alloys. *Acta Materialia* **2001**, *49* (9), 1589–1598.

(6) Was, G. S.; Ampornrat, P.; Gupta, G.; Teysseyre, S.; West, E. A.; Allen, T. R.; Sridharan, K.; Tan, L.; Chen, Y.; Ren, X. Corrosion and Stress Corrosion Cracking in Supercritical Water. *Journal of Nuclear Materials* **2007**, *371* (1–3), 176–201.

(7) Shimada, M.; Kokawa, H.; Wang, Z. J.; Sato, Y. S.; Karibe, I. Optimization of Grain Boundary Character Distribution for Intergranular Corrosion Resistant 304 Stainless Steel by Twin-Induced Grain Boundary Engineering. *Acta Materialia* **2002**, *50* (9), 2331–2341.

(8) Kleinert, M.; Waibel, H.-F.; Engelmann, G. E.; Martin, H.; Kolb, D. M. Co Deposition on Au(111) and Au(100) Electrodes: An in Situ STM Study. *Electrochimica Acta* **2001**, *46* (20), 3129–3136. https://doi.org/10.1016/S0013-4686(01)00604-1.

(9) Schreiber, A.; Rosenkranz, C.; Lohrengel, M. M. Grain-Dependent Anodic Dissolution of Iron. *Electrochimica Acta* **2007**, *52* (27), 7738–7745. https://doi.org/10.1016/j.electacta.2006.12.062.

(10) Waibel, H.-F.; Kleinert, M.; Kibler, L. A.; Kolb, D. M. Initial Stages of Pt Deposition on Au(111) and Au(100). *Electrochimica Acta* **2002**, *47* (9), 1461–1467. https://doi.org/10.1016/S0013-4686(01)00861-1.

(11) Wiame, F.; Maurice, V.; Marcus, P. Initial Stages of Oxidation of Cu(111). *Surface Science* **2007**, *601* (5), 1193–1204. https://doi.org/10.1016/j.susc.2006.12.028.

(12) Shahryari, A.; Szpunar, J. A.; Omanovic, S. The Influence of Crystallographic Orientation Distribution on 316LVM Stainless Steel Pitting Behavior. *Corrosion Science* **2009**, *51* (3), 677–682. https://doi.org/10.1016/j.corsci.2008.12.019.

(13) Was, G. S.; Teysseyre, S.; Jiao, Z. Corrosion of Austenitic Alloys in Supercritical Water. *Corrosion* **2006**, *62* (11), 989–1005.

(14) Jiao, Z.; Was, G. Oxidation of a Proton-Irradiated 316 Stainless Steel in Simulated BWR NWC Environment. In *Proceedings of the 15th International Conference on Environmental Degradation of Materials in Nuclear Power Systems—Water Reactors*; Springer, 2011; pp 1329–1338.

(15) Wang, S.; Wang, J. Effect of Grain Orientation on the Corrosion Behavior of Polycrystalline Alloy 690. *Corrosion Science* **2014**, *85*, 183–192. https://doi.org/10.1016/j.corsci.2014.04.014.

(16) Song, G.-L.; Mishra, R.; Xu, Z. Crystallographic Orientation and Electrochemical Activity of AZ31 Mg Alloy. *Electrochemistry Communications* **2010**, *12* (8), 1009–1012. https://doi.org/10.1016/j.elecom.2010.05.011.
(17) Miao, Y.; Mo, K.; Yao, T.; Lian, J.; Fortner, J.; Jamison, L.; Xu, R.; Yacout, A. M. Correlation between Crystallographic Orientation and Surface Faceting in UO2. *Journal of Nuclear Materials* **2016**, *478*, 176–184. https://doi.org/10.1016/j.jnucmat.2016.05.044.
(18) Fushimi, K.; Miyamoto, K.; Konno, H. Anisotropic Corrosion of Iron in PH 1 Sulphuric Acid. *Electrochimica Acta* **2010**, *55* (24), 7322–7327. https://doi.org/10.1016/j.electacta.2010.07.044.
(19) Brito, P.; Schuller, É.; Silva, J.; Campos, T. R.; Araújo, C. R. de; Carneiro, J. R. Electrochemical Corrosion Behaviour of (100), (110) and (111) Fe3Al Single Crystals in Sulphuric Acid. *Corrosion Science* **2017**, *126*, 366–373. https://doi.org/10.1016/j.corsci.2017.05.029.
(20) Wang, S.; Wang, J. Effect of Grain Orientation on the Corrosion Behavior of Polycrystalline Alloy 690. *Corrosion Science* **2014**, *85*, 183–192. https://doi.org/10.1016/j.corsci.2014.04.014.
(21) Wang, W.; Alfantazi, A. Correlation between Grain Orientation and Surface Dissolution of Niobium. *Applied Surface Science* **2015**, *335*, 223–226. https://doi.org/10.1016/j.apsusc.2015.01.208.
(22) Bachmann, F.; Hielscher, R.; Schaeben, H. Texture Analysis with MTEX – Free and Open Source Software Toolbox https://www.scientific.net/SSP.160.63 (accessed Aug 31, 2019). https://doi.org/10.4028/www.scientific.net/SSP.160.63.
(23) Bachmann, F.; Hielscher, R.; Schaeben, H. Grain Detection from 2d and 3d EBSD Data—Specification of the MTEX Algorithm. *Ultramicroscopy* **2011**, *111* (12), 1720–1733. https://doi.org/10.1016/j.ultramic.2011.08.002.
(24) Bunge, H.-J. *Texture Analysis in Materials Science: Mathematical Methods*; Elsevier, 2013.
(25) Nečas, D.; Klapetek, P. Gwyddion: An Open-Source Software for SPM Data Analysis. *centr.eur.j.phys.* **2012**, *10* (1), 181–188. https://doi.org/10.2478/s11534-011-0096-2.
(26) Dong, S.; La Plante, E. C.; Chen, X.; Torabzadegan, M.; Balonis, M.; Bauchy, M.; Sant, G. Steel Corrosion Inhibition by Calcium Nitrate in Halide-Enriched Completion Fluid Environments. *npj Materials Degradation* **2018**, *2* (1), 32.
(27) Aydoğdu, G. H.; Aydinol, M. K. Determination of Susceptibility to Intergranular Corrosion and Electrochemical Reactivation Behaviour of AISI 316L Type Stainless Steel. *Corrosion Science* **2006**, *48* (11), 3565–3583.
(28) Was, G. S.; Andresen, P. L. Irradiation-Assisted Stress-Corrosion Cracking in Austenitic Alloys. *JOM* **1992**, *44* (4), 8–13.
(29) McCafferty, E. Introduction to Corrosion Science. 2010. *Alexandria: Springer*.
(30) Santamaria, M.; Di Franco, F.; Di Quarto, F.; Pisarek, M.; Zanna, S.; Marcus, P. Photoelectrochemical and XPS Characterisation of Oxide Layers on 316L Stainless Steel Grown in High-Temperature Water. *Journal of Solid State Electrochemistry* **2015**, *19* (12), 3511–3519.

(31) Guo, P.; La Plante, E. C.; Wang, B.; Chen, X.; Balonis, M.; Bauchy, M.; Sant, G. Direct Observation of Pitting Corrosion Evolutions on Carbon Steel Surfaces at the Nano-to-Micro-Scales. *Scientific reports* **2018**, *8* (1), 7990.
(32) Panossian, Z.; Almeida, N. L. de; Sousa, R. M. F. de; Pimenta, G. de S.; Marques, L. B. S. Corrosion of Carbon Steel Pipes and Tanks by Concentrated Sulfuric Acid: A Review. *Corrosion Science* **2012**, *58*, 1–11. https://doi.org/10.1016/j.corsci.2012.01.025.
(33) Galal, A.; Atta, N. F.; Al-Hassan, M. H. S. Effect of Some Thiophene Derivatives on the Electrochemical Behavior of AISI 316 Austenitic Stainless Steel in Acidic Solutions Containing Chloride Ions: I. Molecular Structure and Inhibition Efficiency Relationship. *Materials Chemistry and Physics* **2005**, *89* (1), 38–48. https://doi.org/10.1016/j.matchemphys.2004.08.019.
(34) Lin, C. C. A Review of Corrosion Product Transport and Radiation Field Buildup in Boiling Water Reactors. *Progress in Nuclear Energy* **2009**, *51* (2), 207–224.
(35) Clarke, W. L.; Cowan, R. L.; Walker, W. L. Intergranular Corrosion of Stainless Alloys. *ASTM STP* **1978**, *656*, 99.
(36) AC11041738, A. *Standard Practices for Detecting Susceptibility to Intergranular Attack in Austenitic Stainless Steels*; ASTM Internat., 2013.
(37) Ji, G.; Li, F.; Li, Q.; Li, H.; Li, Z. A Comparative Study on Arrhenius-Type Constitutive Model and Artificial Neural Network Model to Predict High-Temperature Deformation Behaviour in Aermet100 Steel. *Materials Science and Engineering: A* **2011**, *528* (13), 4774–4782. https://doi.org/10.1016/j.msea.2011.03.017.
(38) He, A.; Xie, G.; Zhang, H.; Wang, X. A Comparative Study on Johnson–Cook, Modified Johnson–Cook and Arrhenius-Type Constitutive Models to Predict the High Temperature Flow Stress in 20CrMo Alloy Steel. *Materials & Design (1980-2015)* **2013**, *52*, 677–685. https://doi.org/10.1016/j.matdes.2013.06.010.
(39) Peng, W.; Zeng, W.; Wang, Q.; Yu, H. Comparative Study on Constitutive Relationship of As-Cast Ti60 Titanium Alloy during Hot Deformation Based on Arrhenius-Type and Artificial Neural Network Models. *Materials & Design* **2013**, *51*, 95–104. https://doi.org/10.1016/j.matdes.2013.04.009.
(40) Vitos, L.; Ruban, A. V.; Skriver, H. L.; Kollár, J. The Surface Energy of Metals. *Surface Science* **1998**, *411* (1), 186–202. https://doi.org/10.1016/S0039-6028(98)00363-X.
(41) Ma, F.; Xu, K.-W. Using Dangling Bond Density to Characterize the Surface Energy of Nanomaterials. *Surface and Interface Analysis* **2007**, *39* (7), 611–614. https://doi.org/10.1002/sia.2562.
(42) Eberhart, J. G.; Horner, S. Bond-Energy and Surface-Energy Calculations in Metals. *J. Chem. Educ.* **2010**, *87* (6), 608–612. https://doi.org/10.1021/ed100189v.
(43) Galanakis, I.; Papanikolaou, N.; Dederichs, P. H. Applicability of the Broken-Bond Rule to the Surface Energy of the Fcc Metals. *Surface Science* **2002**, *511* (1), 1–12. https://doi.org/10.1016/S0039-6028(02)01547-9.
(44) Galanakis, I.; Bihlmayer, G.; Bellini, V.; Papanikolaou, N.; Zeller, R.; Blügel, S.; Dederichs, P. H. Broken-Bond Rule for the Surface Energies of Noble Metals. *EPL* **2002**, *58* (5), 751. https://doi.org/10.1209/epl/i2002-00413-7.

(45) Jiang, Q.; Lu, H. M.; Zhao, M. Modelling of Surface Energies of Elemental Crystals. *J. Phys.: Condens. Matter* **2004**, *16* (4), 521–530. https://doi.org/10.1088/0953-8984/16/4/001.
(46) Zhou, Z.-Y.; Tian, N.; Li, J.-T.; Broadwell, I.; Sun, S.-G. Nanomaterials of High Surface Energy with Exceptional Properties in Catalysis and Energy Storage. *Chem. Soc. Rev.* **2011**, *40* (7), 4167–4185. https://doi.org/10.1039/C0CS00176G.
(47) Xu, L.; Liang, H.-W.; Yang, Y.; Yu, S.-H. Stability and Reactivity: Positive and Negative Aspects for Nanoparticle Processing. *Chem. Rev.* **2018**, *118* (7), 3209–3250. https://doi.org/10.1021/acs.chemrev.7b00208.
(48) Liu, H.-T.; Armitage, A. F.; Woodruff, D. P. Anisotropy of Initial Oxidation Kinetics of Nickel Single Crystal Surfaces. *Surface science* **1982**, *114* (2–3), 431–444.
(49) Hua, Z.; An, B.; Iijima, T.; Gu, C.; Zheng, J. The Finding of Crystallographic Orientation Dependence of Hydrogen Diffusion in Austenitic Stainless Steel by Scanning Kelvin Probe Force Microscopy. *Scripta Materialia* **2017**, *131*, 47–50.